The Structural Properties and Photoelectrocatalytic Response of Mn-Doped Hematite Photoanodes Prepared via a Modified Electrodeposition Approach

Pannan I. Kyesmen,*[a, b] Joseph Simfukwe,[c] Peverga R. Jubu,[b] Adedapo O. Adeola,[d] and Mmantsae Diale*[a]

The concept of nanostructuring and doping of hematite (α-Fe_2O_3) photoanodes have been widely engaged towards improving their photoelectrocatalytic (PEC) response. Here, a $FeCl_3$-based solution was modified with 0–10% polyethylene glycol (PEG) 400 and used as an electrolyte for the electrodeposition of nanostructured α-Fe_2O_3 thin films. The electrolyte containing 10% PEG was further used to prepare Mn-doped α-Fe_2O_3 films by adding 1, 3, 6, and 10% of $MnCl_2.4H_2O$ with respect to the molarity of $FeCl_3$. The addition of 10% PEG into the electrolyte limited particle agglomeration and yielded the best PEC response among the pristine films. The 3% Mn-doped α-Fe_2O_3 photoanodes produced the highest photocurrent, yielding 2.2 and 6.1-fold photocurrent enhancement at 1.23 V and 1.5 V vs. RHE respectively, over the pristine films. The improved PEC response is linked to the reduced particle agglomeration and improved charge transport properties observed for the films. Density functional theory (DFT) calculations of the formation energies yielded negative values for the Mn-doped α-Fe_2O_3, which implies that the materials are thermodynamically stable after doping. This work introduces a new pathway for the electrodeposition of doped α-Fe_2O_3 films and underscores the roles of Mn-doping in boosting their PEC response.

1. Introduction

Hydrogen (H_2) is one of the best chemical fuels because of its high energy density and the generation of the by-product of water after undergoing an oxidation reaction. H_2 has many applications as an energy carrier for the aviation industry, can be converted to electricity for home consumption, and can be used as fuel for hydrogen-based automobiles. No wonder, it is generally regarded as the fuel of the future. There are several means of producing this fascinating fuel, which include the steam reforming of methane,[1] gasification of biomass,[2] and solar water splitting via photoelectrocatalysis.[3] Solar water splitting is a renewable and sustainable means for generating H_2, owing to the abundance of solar radiation and its limited effects on our environment. α-Fe_2O_3 is one of the vastly investigated photoanodes for application in the PEC splitting of water for H_2 generation. This is mainly because of its suitable bandgap (~2.0 eV) and stability in solution.[4] However, the major drawback of applying α-Fe_2O_3 in water splitting is its low conductivity, poor oxygen evolution kinetics, and inadequate conduction band position for H_2 evolution.[5] Nanostructuring,[6] doping,[7] and heterojunction design[8] are among the top approaches engaged by researchers towards boosting the PEC properties of α-Fe_2O_3.

Nanostructuring of α-Fe_2O_3 photoelectrodes involves the development of nanoscale structures with various morphological properties such as shapes, sizes, porosity, and particle agglomeration among other surface characteristics. Nanostructuring has been used to promote the charge transport and PEC properties of α-Fe_2O_3, without compromising its light absorption, given its low absorption coefficient. Different methods, such as atomic layer deposition,[9] spray pyrolysis,[10] chemical vapor deposition,[6a] hydrothermal,[11] and electrodeposition[12] techniques, have been employed to fabricate nanostructured α-Fe_2O_3 films, which are largely geared toward developing films with suitable surfaces for photocatalytic applications. The electrodeposition technique is one of the fast, and easy methods of preparing large surface areas of α-Fe_2O_3 photoelectrodes. It also offers the versatility of adjusting the composition of the electrolyte solution for film deposition, which allows for tuning the intrinsic and surface properties of α-Fe_2O_3. However, one of the commonly reported challenges of this approach is the agglomeration of the nanostructures, which often limits photon absorption and PEC efficiency.[13] Yilmaz

[a] Dr. P. I. Kyesmen, Prof. M. Diale
University of Pretoria, Department of Physics, Private Bag X20, Hatfield 0028, South Africa
E-mail: pannan.kyesmen@tuks.co.za
mmantsae.diale@up.ac.za
[b] Dr. P. I. Kyesmen, Dr. P. R. Jubu
Department of Physics, Joseph Sarwuan Tarka University Makurdi (formerly, University of Agriculture Makurdi)
[c] Dr. J. Simfukwe
Copperbelt University, Physics Department, Riverside, Kitwe 10101, Zambia
[d] Dr. A. O. Adeola
Department of Chemistry and Biochemistry and the Centre for NanoScience Research, Concordia University, Montréal, QC, H4V 1R6, Canada

Supporting information for this article is available on the WWW under https://doi.org/10.1002/celc.202400348

et al. 2015, used a modified electrodeposition technique to prepare α-Fe_2O_3 photoanodes. They observed the aggregation of the nanoparticles across the film's surface, regardless of the $FeCl_2$-based precursor concentration, and achieved a low optimum photocurrent of 23 μA/cm^2.[13a] In another study, aggregates of compact nanostructures for α-Fe_2O_3 films that were prepared using the electrodeposition method were obtained. The aggregation of the particles limited the film's porosity, photon absorption, and PEC response.[14] Fu *et al.* 2014, prepared α-Fe_2O_3 photoanodes using the electrodeposition method and observed the aggregation of nanorods on the film's surface, which limited their PEC activity during photoelectrocatalysis. The nanorods aggregation was reduced through ethylene glycol addition into the $FeCl_2$-based electrolyte, which acted as a capping agent, improving the PEC performance of the films.[15]

Numerous materials such as ethylene glycol, polyethylene glycol (PEG), polyvinyl chloride (PVP), and starch could be used to act as surfactants or templating agents in the solution-based synthesis of nanomaterials to limit particle aggregation.[16] In the case of hematite's nanomaterials synthesis, it has been previously shown in a force hydrolysis fabrication of the material that PEG can adsorb on FeOOH even at room temperature.[17] The adsorb PEG can be removed by rinsing with water and the resulting FeOOH can be sintered to obtain less aggregated hematite nanoparticles. The adsorb PEG on FeOOH can act as a caping or templating agent that helps limit the aggregation of the nanoparticles.[15,17] For many electrodeposition of hematite films on FTO, FeOOH is usually deposited before sintering at 450–550 C to obtain crystalline hematite.[12,18] However, the addition of PEG in the electrolyte to act as a capping agent in the electrodeposition of hematite films has not been exploited.

Doping is another strategy that has been widely used to improve the intrinsic properties of α-Fe_2O_3 films, for PEC applications. This strategy is mainly engaged in materials development towards boosting the conductivity of photocatalysts with poor charge transport behavior such as α-Fe_2O_3. Theoretical calculations using Density Functional Theory (DFT) and experimental studies point to the reduction of the effective mass of electrons and the enhancement of charge carrier concentration after doping, boosting the conductivity of the material. α-Fe_2O_3 has been doped with various metals such as Sn,[19] Cu,[20] Mn,[21] and Ce[22] to improve its conductivity and light harvesting capacity in some cases. Mn is one of the suitable dopants of α-Fe_2O_3 because of its similar atomic radii with Fe, which is not expected to cause any significant distortion in the crystal structure of α-Fe_2O_3, ensuring its stability in electrolytes during catalytic applications. Also, doping of α-Fe_2O_3 with Mn can significantly boost its charge carrier's concentration, thereby enhancing its conductivity and PEC properties. Despite these advantages, Mn has been sparsely engaged in the doping of α-Fe_2O_3 photoanodes for PEC applications. Gurudayal et al. 2014, used the hydrothermal technique to prepare Mn-doped α-Fe_2O_3 nanorods, enhancing the charge carrier's concentration and photocurrent of the pristine films by an order of 10^2 and 75% respectively. However, the fabricated Mn-doped α-Fe_2O_3 films were sintered at 750 °C for 20 mins after pre-annealing at 500 °C, which is likely to result in the unintentional doping of the samples by the Sn content of the fluorine-doped tin oxide (FTO) substrates used for the film's preparation through thermal diffusion. So, the PEC response reported could also be due to Mn and Sn co-doping of hematite.[21] The Mn-doping of nanostructured α-Fe_2O_3 photoanodes using the widely engaged electrodeposition technique has not been reported based on known literature.

Here, a modified electrodeposition technique was used to prepare Mn-doped- α-Fe_2O_3 for PEC water splitting. $FeCl_3$-based solution used as electrolyte for the electrodeposition of nanostructured α-Fe_2O_3 photoanodes was modified with 0, 2.5, 5.0, and 10% of PEG 400 to act as a capping agent towards limiting the aggregation of the nanoparticles. 10% PEG yielded the least particle agglomeration and the best photoresponse among the pristine films. Hence, the electrolyte containing 10% PEG was further used to prepare Mn-doped α-Fe_2O_3 films by adding 1, 3, 6, and 10% of $MnCl_2.4H_2O$ with respect to the molarity of $FeCl_3$. Mn-doping with the 3% Mn ion source notably increased the charge carrier concentration of the α-Fe_2O_3 photoanodes, producing 2.2 and 6.1 times more photocurrent than the pristine films at 1.23 and 1.5 V vs. RHE respectively. This project introduces a new pathway for the preparation of pristine and doped electrodeposited α-Fe_2O_3 nanoparticles, for the enhancement of PEC activity. It also showcases for the first time, based on known literature, the impact of Mn-doping on the PEC response of pristine electrodeposited α-Fe_2O_3 photoanodes. This research also opens the room for exploring the efficacy of capping agents in the preparation of electrodeposited nanostructured films to limit particle agglomeration.

2. Results and Discussion

2.1. Structural studies

The XRD studies were done within 2θ values of 20—70 degrees on the pristine and doped α-Fe_2O_3 films to extract their structural data, and the results are given in Figure S1 of the supplementary data and Figure 1 respectively. The patterns of the XRD results for the pristine and Mn-doped α-Fe_2O_3 films disclosed notable diffraction peaks at (104) and (110) planes, indicating the formation of the rhombohedral crystal structure of α-Fe_2O_3 with lattice parameters a = b = 5.032, c = 13.733; $R\bar{3}c$ symmetry group. The pattern also presents weak diffraction peaks at (012), (113), (116), (024), (018), (214) and (300) planes associated with those of α-Fe_2O_3 based on the JCPDS file no. 33-0664. The samples prepared were of good quality since the peaks of other oxides of Fe and Mn were not seen in the diffraction pattern of the films. Analysis of the 2θ values obtained for the (104) and (110) peaks did not reveal any significant shift in the peak positions of (104) and (110) planes for the pristine and 1%-Mn-doped α-Fe_2O_3 samples. Further doping of the 10%-PEG films with 3%–10% Mn resulted in a noticeable shift in the peak positions of the (104) and (110) planes to lower 2θ values by 0.22–0.24 and 0.20–0.24 degrees,

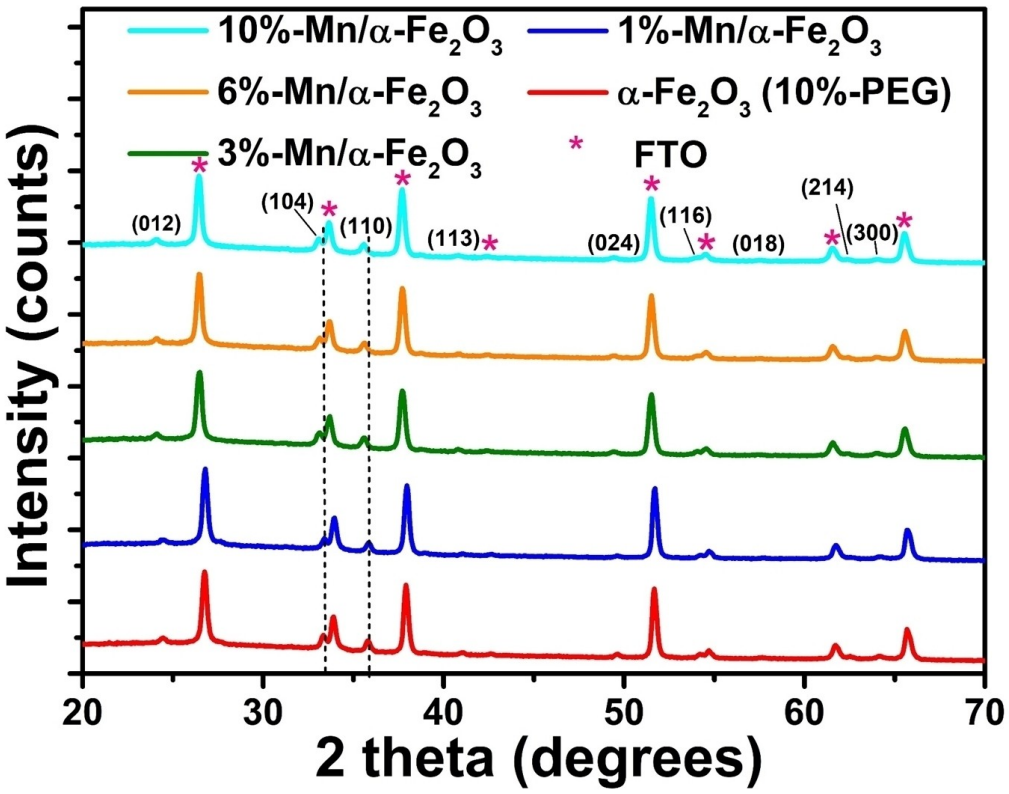

Figure 1. XRD patterns of electrodeposited α-Fe_2O_3 films doped with Mn.

respectively. The change in the position of the XRD peaks was due to Mn-doping of the pristine α-Fe_2O_3 films and proof that Mn was incorporated into the lattice structure of α-Fe_2O_3. Depending on the preparation process, the dopant, and the doping level, the lattice volume of α-Fe_2O_3 may decrease or increase causing the XRD peaks to move to higher or lower 2θ positions respectively.[20] Cu-doped α-Fe_2O_3 films have been reported to exhibit a shift in the XRD peaks to both lower[23] and higher[20,24] 2θ values. The shifts in the XRD peaks to lower 2θ values observed for the Mn-doped-α-Fe_2O_3 samples were due to the increase in the lattice volume of the doped samples resulting from the higher atomic radii of Mn^{2+} (r = 0.083 nm)[25] compared to that of F^{3+} (r = 0.064 nm).[20] Similar observations have been made for Cu^{2+},[20] Ce^{3+} Ce^{4+},[22] and In^{3+}[7] doped α-Fe_2O_3 samples in literature. The replacement of Fe^{3+} with Mn^{2+} resulted in charge imbalance and to make up for this, some oxygen vacancies were created, which caused the lattice size to increase, shifting the XRD peak positions to lower 2θ values.

The (110) peaks were used to evaluate the full width at half maximum (FWHM) and the crystal size (D) values of the pristine and α-Fe_2O_3 films doped with Mn by engaging the Debye-Scherrer approximation. In addition, the dislocation density (α) and microstrain (ε) values of the films were estimated using Williamson and Smallman's method to obtain additional microstructural information for the samples.[26] The results obtained for D, α, and ε of the films are presented in Figure 2(a), (b), and (c) respectively, and in Table S1. The crystal size of the pristine films did not show any significant change with the addition of PEG into the electrolyte solution. However, doping of the α-Fe_2O_3 films with Mn resulted in a consistent decrease in the crystal size values with increasing doping concentration. A similar drop in the crystallite size of materials due to doping has been reported in the literature.[20,27] Identically, the addition of PEG into the electrolyte did not show any recognizable influence on the dislocation density and the microstrain values evaluated for the pristine films. The dislocation density present in the doped samples was continually enhanced with an increase in the Mn doping concentration. This is explained by the lattice distortion that resulted from the substitution of F^{3+} with Mn^{2+} in the structure of α-Fe_2O_3, which is comparable to an earlier observation for PbO doped with Mn.[28] The microstrain of the doped samples also became larger relative to the pristine films and is attributed to the lattice expansion that occurred because of the substitution of Fe^{3+} with Mn^{2+} in the crystal lattice. This also affirms the broadening of the XRD peaks of the doped samples and the decreasing crystal sizes observed for the films.

The Raman spectra of the prepared α-Fe_2O_3 films and those doped with Mn were obtained to study their phonon vibrational modes and gain more structural information about the samples. The Raman spectra of the samples are given in Figure 3(a) and (b) for the pristine and Mn-doped samples respectively. The spectra of all the samples verified the $2A_{1g}$ and $5E_g$ phonon modes of α-Fe_2O_3. The vibrational modes of other oxides of Fe or Mn were not observed in all the samples, further asserting the high purity of the prepared films, supporting the

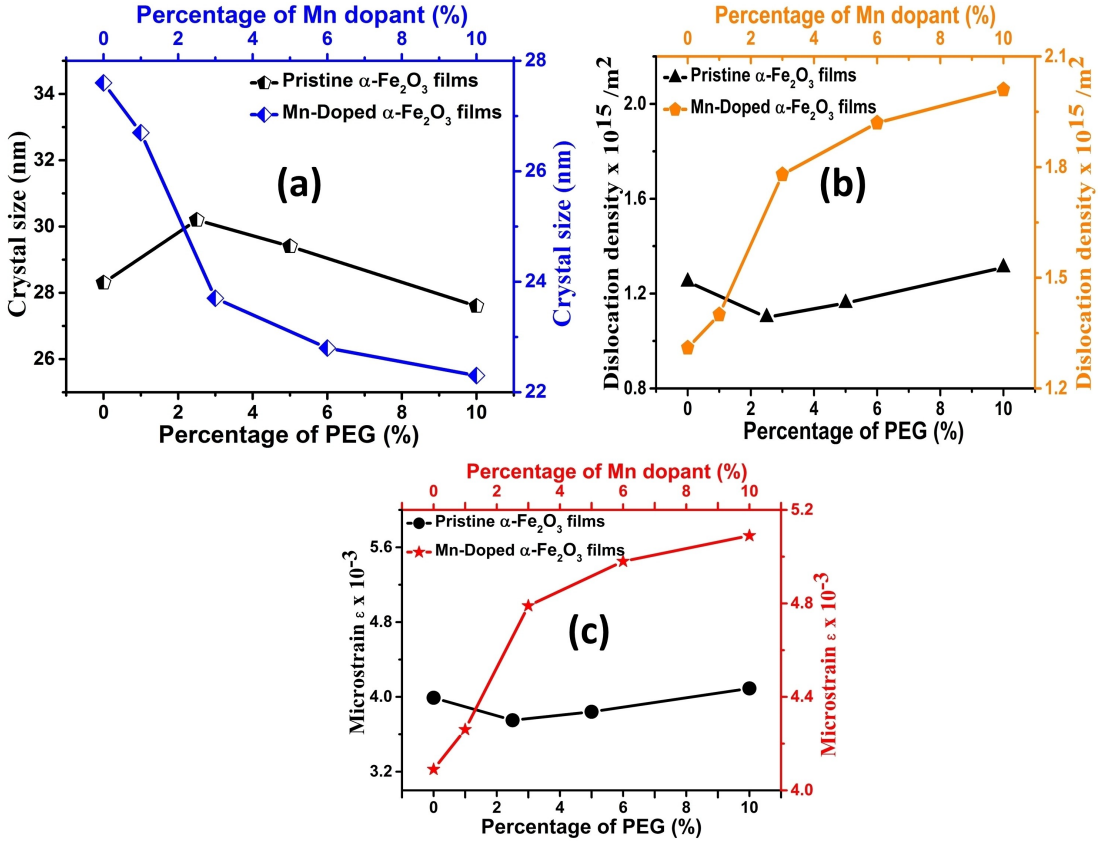

Figure 2. The (a) crystal size, (b) dislocation density, and (c) microstrain for the pristine α-Fe_2O_3 films and ones doped with Mn.

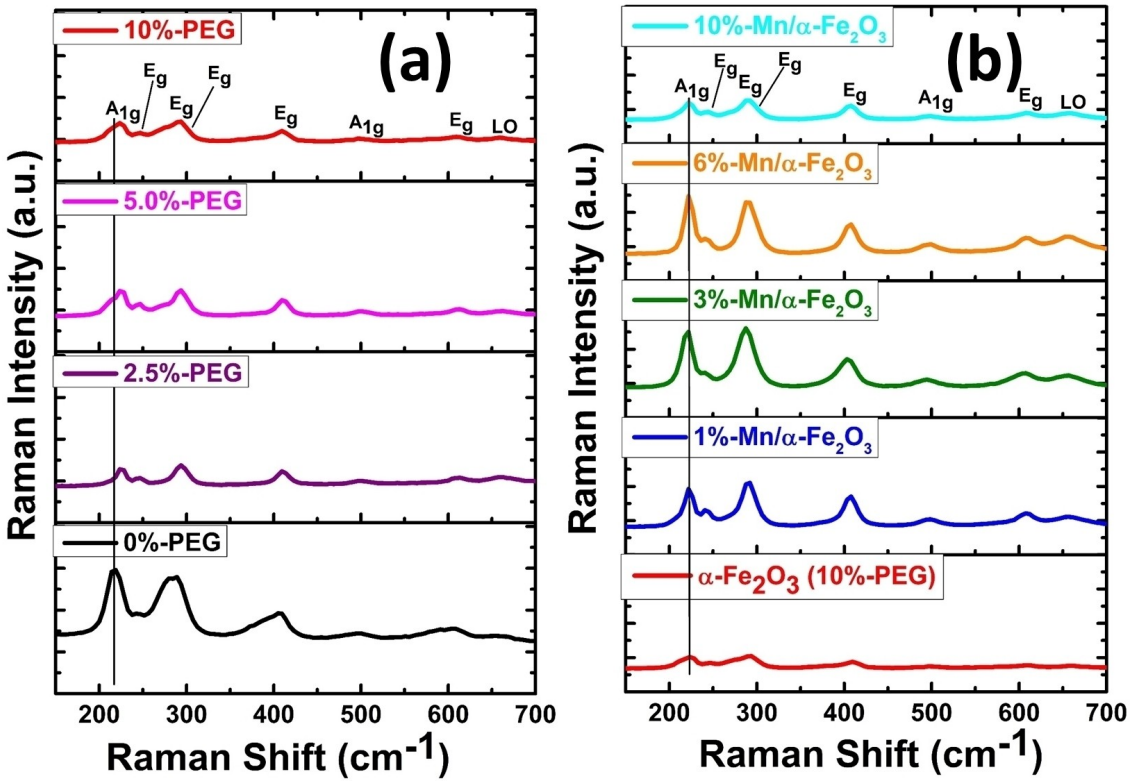

Figure 3. Raman spectra of (a) undoped and (b) α-Fe_2O_3 films doped with Mn.

successful incorporation of Mn into the lattice structure of α-Fe_2O_3, in agreement with the XRD results. The Raman peak that appeared at 660 and 557 cm^{-1} for the pristine and doped films respectively are the infrared active longitudinal optical modes of α-Fe_2O_3 denoted by LO, which is normally made active by the presence of internal strain and local disorder in α-Fe_2O_3 lattice.[29] Hence the LO mode peak is more pronounced in the Raman spectra of the Mn-doped films because of the increased lattice disorder caused by the doping effect.

Furthermore, the peak positions and broadening of the first A_{1g} and E_g modes of the Raman spectra of the samples were extracted through the Lorentzian fitting and deconvolution of the peaks. The results are given in Figure 4 and Figure S2 for the doped and undoped α-Fe_2O_3 samples respectively, and in Table S2. The results disclosed a blue shift of the Raman peak positions with the addition of PEG into the electrolyte that was used for film deposition. This cannot be associated with quantum confinement since the crystal size of the nanoparticles was similar for all the pristine films.[30] Also, particle agglomeration was reduced with the addition of PEG to the electrolyte and it is not expected to result in the blue shifting of the peak positions.[31] So, the likely reason for the observed blue shift of the Raman peak positions is the reduction in the film's thickness with the addition of PEG into the electrolyte (Figure S4), in line with a previous observation.[32] No shift in the Raman peak positions of Mn-doped films was noticed with respect to the ones of the pristine 10%-PEG sample. For the doped films, the blue shifting of the Raman peak positions was anticipated with the reduction of the particle size of Mn-doped films due to quantum confinement.[30] On the other hand, red-shifting of the peaks arising from some impurity-induced scattering due to Mn doping of the α-Fe_2O_3 may have occurred, similar to a reported observation for Mn- and Co-doped ZnO.[33] These two effects may have compensated for each other, resulting in no noticeable change observed in the Raman peak positions of the doped films. The broadening of the peaks, represented by their FWHM values did not show any distinct pattern for both the undoped and doped samples.

2.2. Morphological and Elemental Content Analysis

The surface micrographs of the pristine α-Fe_2O_3 films are given in Figure 5(a)–(d) for the 0%- to 10%-PEG samples, revealing spherical nanoparticles for all the samples. The films fabricated using the electrolyte that contained 0% PEG revealed highly agglomerated nanoparticles which appeared to be loosely attached to the film's surfaces. In solar photoelectrocatalysis, high particle agglomeration on photoelectrode's surfaces can serve as recombination sites for charge carriers and negatively affect their catalytic response.[34] Further increase of the PEG content in the electrolyte notably decreased the extent of the nanoparticle's agglomeration on the surface of the films. The 10%-PEG films yielded a more uniform surface with the least particle agglomeration. As earlier mentioned, it has been reported in a force hydrolysis synthesis of hematite nanoparticles that PEG can adsorb onto FeOOH even at room temperature.[17] In this work, the PEG content in the modified electrolyte is also proposed to have been adsorbed by the FeOOH deposited on the substrates during the electrodeposition process, which acted as a capping agent that helped limit the aggregation of the nanoparticles on the film's surface.[15,35] The decreased particle agglomeration and uniform surface observed for the 10%-PEG samples can result in a less rough surface, which sometimes limits PEC activity due to the reduced surface area available for the reactions.[36] However, an increase in the surface roughness of photoelectrodes caused by the aggregation of the nanoparticles is counterproductive in PEC applications. This is because aggregated nanoparticles serve as recombination centers for charge carriers during water

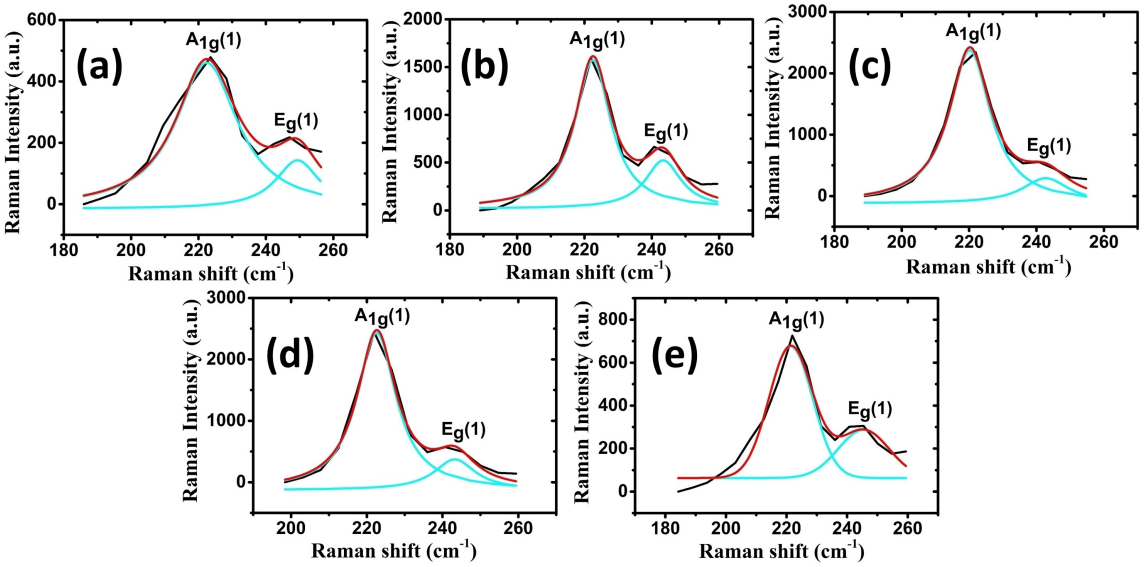

Figure 4. Lorentzian fitting and deconvolution curves for the initial two vibrational modes of the Raman spectra of the a) 10%-PEG pristine sample, and (b) 1%-Mn, (c) 3%-Mn, (d) 6%-Mn, and (e) 10%-Mn doped α-Fe_2O_3 samples.

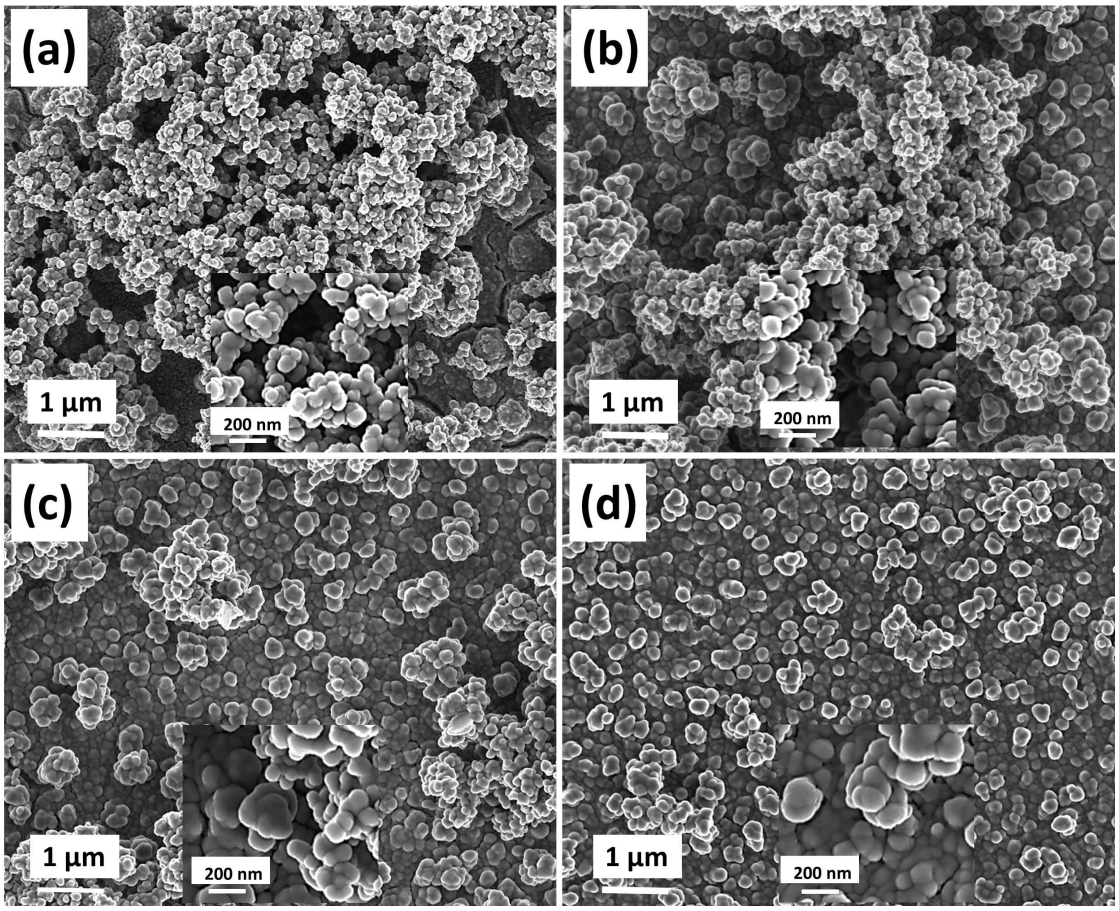

Figure 5. The surface micrographs of pristine α-Fe_2O_3 films for (a) 0%-PEG, (b) 2.5%-PEG, (c) 5.0%-PEG, and (d) 10%-PEG samples.

splitting.[37] The mean particle sizes of the nanoparticles could not be approximated due to high particle agglomeration. The surface morphologies of the Mn-doped α-Fe_2O_3 samples are presented in Figure S3(a)–(d) for the 1–10% Mn-doped films. They also disclosed spherical nanoparticles on their surfaces and limited particle agglomeration that is comparable with those of 10%-PEG samples.

The cross-sectional micrographs of the pristine α-Fe_2O_3 samples, presented in Figure S4 of the supplementary data, were evaluated using the ImageJ tool to calculate their thicknesses. The approximate thickness of the films decreases with increasing concentration of PEG content in the electrolyte used for film deposition. This was because PEG is a non-conductive polymer and its addition into the precursor solution reduces the conductivity of the electrolyte, which limited the electrodeposition of FeOOH onto the FTO substrates, reducing the film's thicknesses. The maximum approximate film thickness of 301 ± 15 nm was obtained for the 0%-PEG sample while the least value of 221 ± 29 nm was evaluated for 10%-PEG α-Fe_2O_3 films. The thicknesses of the Mn-doped films were not evaluated since the same electrolyte used for the preparation of the 10%-PEG samples was used for the film's deposition, and their thicknesses were not expected to vary significantly with doping, similar to previous observations.[21,38]

The results of the EDS mapping conducted on the surface of the Mn-doped α-Fe_2O_3 samples are presented in Figure 6(a)–(d). The mapping confirms the presence and uniform distribution of Fe and O atoms across the doped films, which are the constituent elements of α-Fe_2O_3. The bright areas seen on maps are the regions where some slight particle agglomeration occurred on the surface of the films. The EDS maps also show a homogeneous distribution of Mn across the film's surfaces and further assert the successful incorporation of Mn into the crystal lattice of α-Fe_2O_3. The Sn detected in the maps results from the presence of Sn in the FTO substrates employed for the electrodeposition of the α-Fe_2O_3 films.

2.3. Optical Characteristics

UV–Vis spectroscopy was conducted to ascertain the absorption behavior and the approximate band gap of the pristine and Mn-doped films. The normalized absorption patterns of the samples are shown in Figure 7(a) and (b) for the undoped and Mn-doped α-Fe_2O_3 films respectively. The absorption patterns of the films revealed two distinct peaks at wavelengths of about 404 and 542 nm. The peak at 404 nm corresponds to the ligand field transitions $^6A_1$–$^4E_1$, $^4A_1$, related to the single Fe^{3+} cation while the one at 542 nm is ascribed to the transitions that result

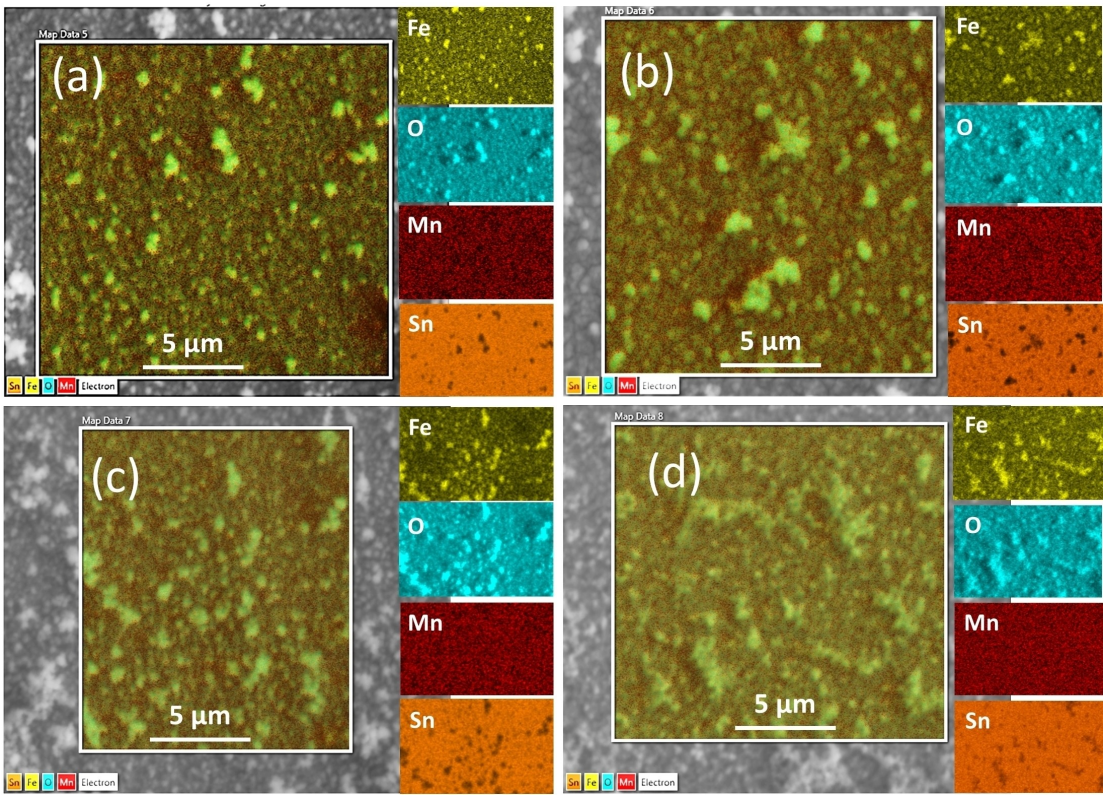

Figure 6. The EDS maps of (a) 1%-Mn, (b) 3%-Mn, (c) 6%-Mn, and (d) 10%-Mn doped α-Fe_2O_3 samples.

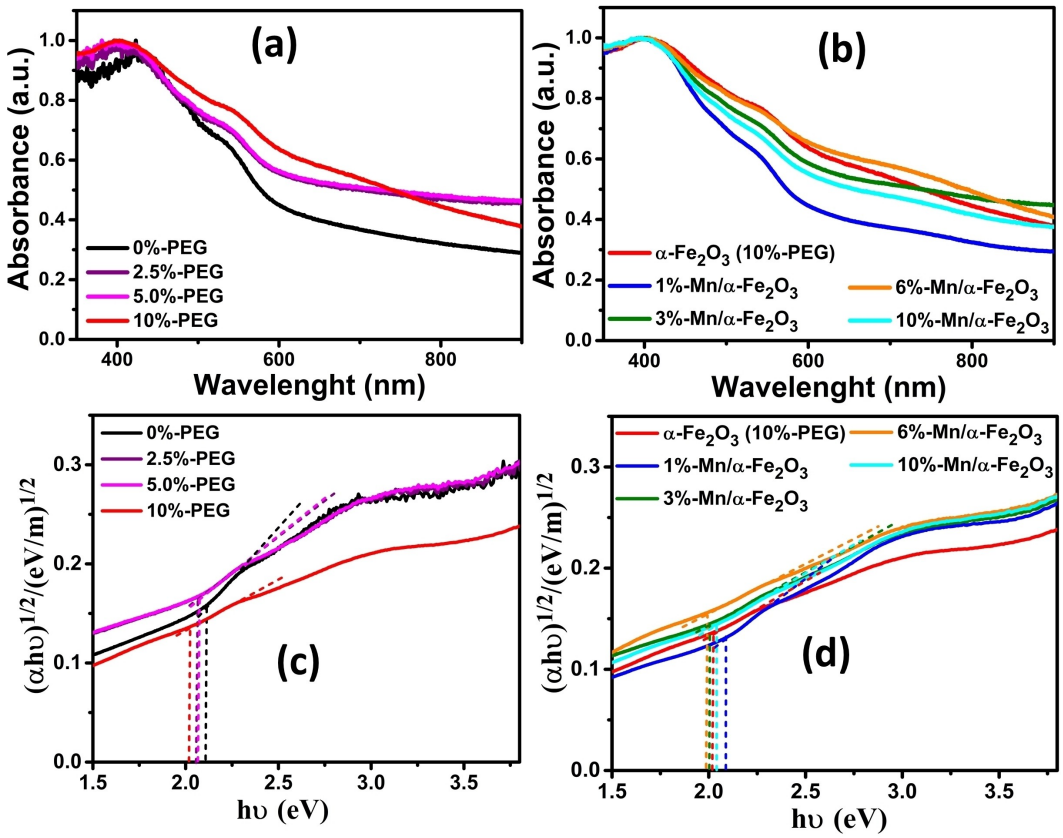

Figure 7. UV–Vis optical absorption of (a) pristine and (b) Mn-doped α-Fe_2O_3 films: (c) and (d) present the Tauc plots for the approximation of the indirect bandgap of the pristine and doped samples, respectively.

from double exciton processes involving Fe^{3+}–Fe^{3+} cation pairs.[39] For the undoped films, the photon absorption appeared to be enhanced with increasing PEG concentration in the electrolyte used for film deposition, regardless of the decreasing film thicknesses. Hence, the 10%-PEG samples exhibited the highest photon absorption within the visible spectrum. The improved absorption observed for the films was attributed to the significant reduction in nanoparticles agglomeration in the films due to the addition of PEG into the electrolyte. The reduced particle agglomeration will increase the light penetration depth and favor light scattering against its diffusion, which leads to the improved absorption pattern observed for the films.[37] Improved photon absorption by photoelectrodes is desired for generating sufficient charge carriers needed for PEC reactions.

The Tauc approximation given in equation S1 of the supplementary data was used to evaluate the indirect bandgap of the pristine and Mn-doped α-Fe_2O_3 films and the results are given in Figure 7(c) and (d) respectively. The bandgap values estimated for the pristine films decrease from 2.11 eV for 0%-PEG samples to 2.02 eV for the 10%-PEG films. This is associated with the improved photon absorption that results from the reduced particle agglomeration on the surface of the samples with increasing PEG concentration in the solution. Mn-doping of the films did not show any noticeable impact on the bandgap of the films as the estimated values for the doped films were within the margin of ±0.03 eV relative to the bandgap of the pristine films. The bandgap values estimated for the prepared films are given in Table S3 of the supplementary information. The bandgap values for the films from the experimental methods align well with the ones obtained theoretically using DFT calculations. Table S4 shows the theoretically calculated bandgap for the pristine and Mn-doped α-Fe_2O_3. The bandgap of the pristine α-Fe_2O_3 system was found to be 2.17 eV, similar to values reported for the material in literature.[40] The DFT calculated bandgap obtained for the Mn-doped α-Fe_2O_3 systems did not show any appreciable difference from the pristine one, in agreement with the experimental results. This could be attributed to the similar electronic structures of Mn and Fe where they both have filed 4 s orbitals and only with electron difference in their 3d orbitals. The band structure for the calculated bandgaps and PDOS are shown in Figure S5((a) and (b)) and Figure S6 for the undoped and doped systems respectively. The relaxed hexagonal structures of the undoped and doped systems are also given in Figure S5 (c) and Figure S7 respectively.

2.4. Electrochemical Response

2.4.1. Mott–Schottky Studies

Mott–Schottky (M–S) studies were performed on the undoped and doped α-Fe_2O_3 films to extract the donor density (N_D) and flat band potential (V_{fb}) values of the photoanodes. The M–S plots for the pristine α-Fe_2O_3 and the ones doped with Mn are presented in Figure 8(a) and (b) respectively. Equation 1 presents the Mott-Schottky relation used to evaluate the V_{fb} and N_D values of the pristine and doped α-Fe_2O_3 samples.

$$\frac{1}{C^2} = \frac{2}{\mathcal{E}_0 \mathcal{E} e A^2 N_D}\left(V - V_{fb} - \frac{KT}{e}\right) \quad (1)$$

where C denotes the capacitance of the space charge region, A represents the electrode's surface area, $\mathcal{E}$ is the dielectric constant and given as 80 for α-Fe_2O_3, $\mathcal{E}_0$ is the vacuum permittivity, e stands for the electronic charge, the applied potential *is* V, K symbolizes the Boltzmann constant, and T denotes the temperature.[41]

The slope (S) obtained for the samples after fitting the linear regions of their M–S plots were fitted to evaluate N_D values for the photoanodes, in line with $S = 2/\mathcal{E}_0 \mathcal{E} e A^2 N_D$, deduced from Equation 2. The positive S values exhibited by the photoanodes prove the n-type semiconducting property for the pristine and doped α-Fe_2O_3 films.[12] The extrapolation of the linear part of the M–S plots intercepts the potential, V-axis at $1/C^2 = 0$, and the values were used to evaluate the V_{fb} of the samples. Furthermore, the approximate valence and conduction band

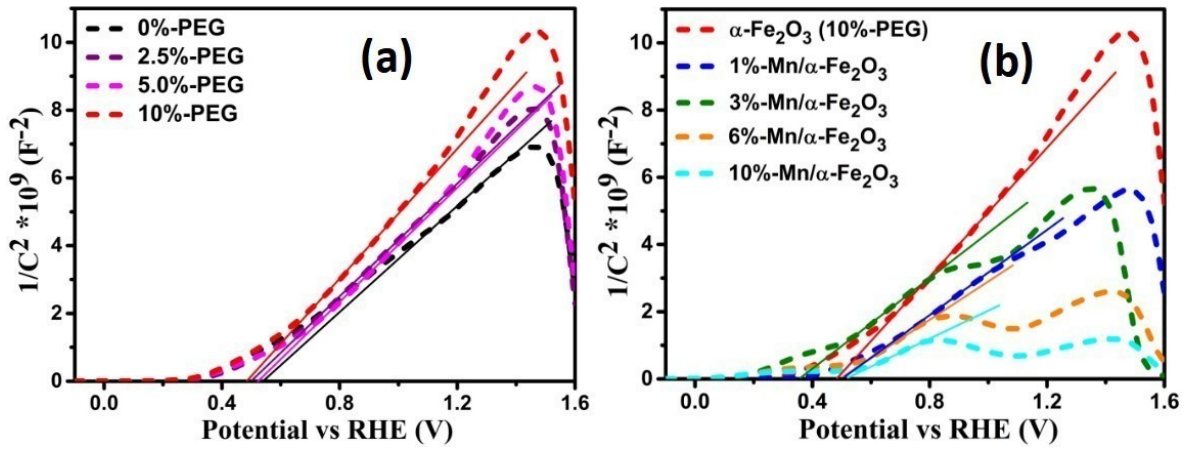

Figure 8. M–S plots for (a) pristine and (b) Mn-doped α-Fe_2O_3 films.

positions, denoted by E_{VB} and E_{CB} respectively, were obtained using the indirect bandgap (Table S3) and the V_{fb} values estimated for the samples. Within the flat band conditions, for an n-type material, the V_{fb} value is equivalent to the fermi level (E_f) of the semiconductor[42] and the E_{CB} is more negative than the E_f value by approximately 0.2.[43] So, given the E_{CB} and E_g of the photoanodes, their E_{VB} was empirically calculated using the basic equation: $E_{VB} = E_{CB} + E_g$. The estimated values of V_{fb}, N_D, E_{CB}, and E_{VB} for the pristine and doped α-Fe_2O_3 samples are displayed in Table 1.

Analysis of the V_{fb} values evaluated for the pristine α-Fe_2O_3 photoanodes slightly decreases with increasing PEG content in the precursor solution used for sample preparation. The V_{fb} of the 10%-PEG was about 0.56 mV more negative when compared to the value estimated for the 0%-PEG films. The reduced V_{fb} observed can be attributed to a decrease in charge recombination occurring on the film's surface due to reduced particle agglomeration. For an n-type material, a more negative V_{fb} will enhance space charge capacitance, limit charge recombination in the bulk of the photoanodes, and boost charge separation at the liquid/solid junction during photoelectrocatalysis.[36a] Doping of the α-Fe_2O_3 films did not improve the V_{fb} values for 1, 6, and 10% Mn-doped samples. However, a significant drop in the V_{fb} value for the 3% Mn-doped sample was observed, producing 123 mV less negative value relative to the pristine 10%-PEG sample, a desired property for PEC applications. In a related response, the E_{CB} value of the 3% Mn-doped sample shifted to a more negative value by 0.13 eV, a key feature for enhancing the efficiency of charge transport in PEC reactions. Meanwhile, the E_{VB} values of the films remain relatively constant for both the pristine and doped α-Fe_2O_3 photoanodes.

Table 1. The flat band potential, donor density, and electronic band positions of pristine and Mn-Doped α-Fe_2O_3 films.

Sample	V_{fb} vs RHE (V) in 1 M NaOH	N_D*10^{19} (cm^{-3})	E_{CB} (eV)	E_{VB} (eV)
0%-PEG	0.513	7.0	0.31	2.42
2.5%-PEG	0.471	6.6	0.27	2.33
5.0%-PEG	0.493	6.5	0.29	2.36
10%-PEG	0.457	5.7	0.26	2.28
1%-Mn-doped	0.477	8.6	0.28	2.33
3%-Mn-doped	0.334	8.0	0.13	2.13
6%-Mn-doped	0.474	9.1	0.27	2.26
10%-Mn-doped	0.481	13.4	0.281	2.32

The N_D values evaluated for the pristine α-Fe_2O_3 films ranged from 5.7–7.0×10^{19} cm^{-3}, similar to the values estimated for them in the literature.[19,44] Doping of the pristine films led to a noticeable improvement in the N_D values. The 10% Mn-doped samples yielded the highest N_D value; about twice the values estimated for the pristine films. An increase in N_D values is an expected consequence of Mn doping of α-Fe_2O_3 films since it provides additional electrons in their conduction band. The improved N_D values will boost the conductivity of the pristine films; crucial for enhancing the PEC activity of α-Fe_2O_3 photoanodes. However, an optimal doping level is necessary as excessive doping concentration can cause unwanted trap states within the bandgap of the films to be formed, that can act as recombination sites for photoexcited charge carriers during photoelectrocatalysis.

2.4.2. Photocurrent Response

The photocurrent obtained for the doped and undoped α-Fe_2O_3 samples are presented in Figure 9(a) and (b) respectively. For the pristine films, the photocurrent density increases with the addition of more PEG content in the solution used for film deposition. The highest value of 0.026 and 0.052 mA/cm^2 at 1.3 and 1.5 V vs. RHE was attained by the 10%-PEG, representing a 1.5 and 2.0 times increase relative to the photoresponse observed for the 0%-PEG photoanodes, respectively. Two key components that can impact the PEC response of the pristine

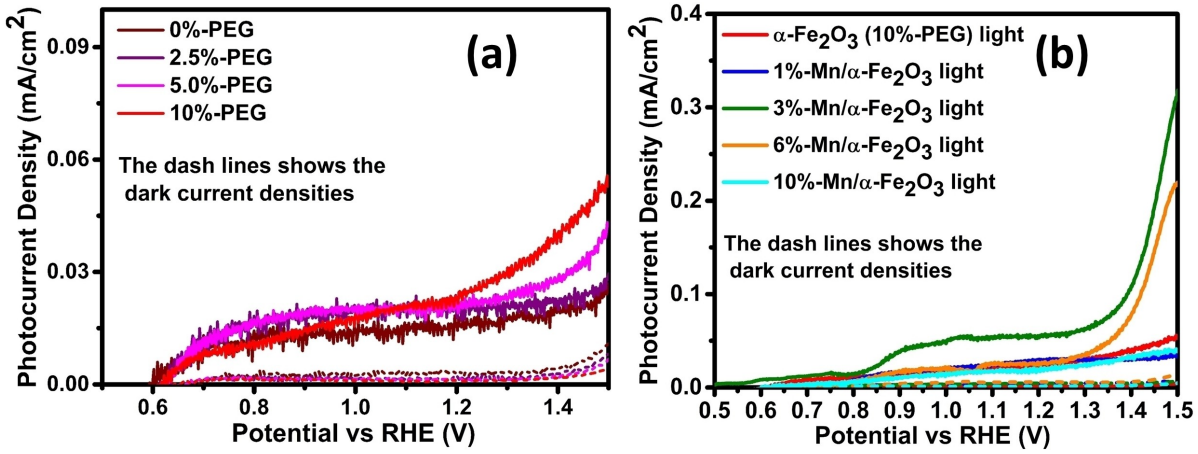

Figure 9. The photocurrent density of (a) undoped and (b) doped α-Fe_2O_3 photoanodes. The dashed lines show the dark current density of the samples presented in a colour that corresponds with that of the photocurrent density plot of the films, respectively.

samples, which include the thickness of the films and particle agglomeration on their surfaces are examined. For α-Fe_2O_3, thin films with over 400 nm thicknesses are desired for sufficient absorption of solar radiation for PEC applications because of their low absorption coefficient.[45] Meanwhile, because of the short hole diffusion length of 2–4 nm[46] of α-Fe_2O_3, if the films are too thick, the charge carriers generated in the bulk of the films during PEC applications will recombine before they get to the surface of the films to initiate PEC reactions. Given this paradox, nanostructured hematite films are produced to allow for the development of thicker films to absorb sufficient solar radiation for PEC reactions while maximizing their charge transport properties.[45a] The optimal film thicknesses of over 300 nm have been reported for α-Fe_2O_3 films in many PEC applications.[45b,47] So, the slight reduction in the thickness of the films with increasing PEG content in the electrolyte was not expected to be responsible for the enhanced PEC response observed for the films. In addition, the optical absorption of the films increases with increasing PEG content and decreasing film thickness, which was earlier attributed to the reduced particle aggregation on the film's surface. The reduction of particle agglomeration on the film's surface not only improved optical absorption but could also enhance their PEC response through reduced surface recombination of charge carriers. This is because agglomerated nanoparticles can act as centers for charge recombination. So, the improved PEC response observed for the 10%-PEG samples is mainly attributed to the reduced aggregation of the nanoparticles on the film's surface, which enhanced photon absorption and reduced the recombination of charge carriers.[34b,37]

The 3% Mn-doped α-Fe_2O_3 photoanodes produced the highest photocurrent of 0.057 mA/cm^2 and 0.32 mA/cm^2 at 1.23 and 1.5 V vs. RHE, representing a 2.2- and 6.1-fold photoresponse enhancement over the pristine films, respectively. The photocurrent onset potential (V_{onset}) observed for the pristine films was relatively constant at about 0.59 V vs. RHE, and the 1%, 6%, and 10% Mn-doped samples did not improve the V_{onset} values. However, the 3% Mn-doped α-Fe_2O_3 yielded a cathodic shift of over 100 mV compared to the value recorded for the pristine films. The improved PEC response observed for the 3% Mn-doped α-Fe_2O_3 is associated with the reduced agglomeration of particles on the film's surface, increased N_D, and the more negative V_{fb} values evaluated for the films. The enhanced N_D values boosted the conductivity of the films,[48] the reduced V_{fb} value helped to decrease the onset potential and promote charge separation,[36a] and the decrease in particle aggregation limited the recombination centers of photogenerated charge carriers.[37] These all culminated in the improved PEC response observed for the 3% Mn-doped α-Fe_2O_3 films. Further doping using 6% and 10% Mn resulted in a decline in the photocurrent density values relative to the response attained by the 3% Mn-doped films. The reduced photocurrent observed for the 1% and 10% Mn-doped films relative to the pristine samples could be linked to the development of high impurity states, which act as recombination centers for photogenerated charge carriers.[49] The optimum photocurrent density value observed for the 3% Mn-doped films compares well with other reported values for doped α-Fe_2O_3 photoanodes prepared at similar annealing temperatures, as seen in Table S5.

The temperature used in treating hematite films during calcination can notably influence their properties.[50] FeOOH usually crystallizes into hematite when treated at sintering temperatures ranging from 450–550 °C.[51] When they are annealed at much higher temperatures, it will cause the formation of larger crystals but can lead to the possible doping of the films by Sn from the FTO substrates. The doped α-Fe_2O_3 samples presented in Table S5 that yielded much higher photocurrent are mostly fabricated at high annealing temperatures of 700 °C and above. The PEC responses of the films were enhanced through improved crystallization and the unintentional doping of the samples by Sn, in cases where FTO substrates or other glass-based conducting substrates are engaged.[52] However, in this work, the prepared Mn-α-Fe_2O_3 films were annealed at 550 °C to help avoid the unintentional doping of the samples by Sn and allow for a more targeted study of the impact of Mn-doping on the PEC response of the photoanodes. Consequently, the crystal sizes of the electrodeposited hematite films produced were limited. This implies that the films produced will exhibit poor conductivity and reduced optical absorption capabilities due to their limited crystallization,[53] thereby limiting their PEC response. This explains the poor photocurrent response of the Mn-doped hematite films presented in this work compared to similar doped films that were sintered at much higher temperatures given in Table S5.

The photostability of the optimized photoanodes; the 10%-PEG pristine α-Fe_2O_3 and the 3%-Mn/α-Fe_2O_3 samples, were investigated in a potential-time scan, and the results are shown in Figure 10. The photoanodes exhibited good stability in a basic electrolyte. The pristine 10%-PEG sample retained over 97.0% while the 3%-Mn/α-Fe_2O_3 photoanodes retained 92.1% of their photocurrent densities after 500 s. The pristine films displayed slightly better photostability when compared to the Mn-doped films, sustaining about 5% more photocurrent. So, the stability of the Mn-α-Fe_2O_3 was not significantly affected by Mn-doping. This is because the atomic radii of Mn^{2+} and F^{3+}[7,25] are identical, and the Mn-doping of hematite did not cause any major structural distortion of films and showed no notable impact on its PEC stability.

Furthermore, the results obtained from the DFT studies yielded additional clarity about the enhanced photocurrent response measured for the Mn-doped samples. The band structure and PDOS are presented in Figure 11(a)–(d) for 2.1% and 4.2% Mn-doped α-Fe_2O_3 systems. The Fermi level of the doped samples was observed to move towards the conduction band minimum (CBM). More so, the distance between the CBM and the Fermi level narrowed from 2.17 eV for the pristine system to 0.66 eV and 0.64 eV for the 2.1% and 4.2% Mn-doped systems respectively. The decrease in the distance between the CBM and the Fermi level leads to an increase in the electron carrier concentration of the Mn-doped systems,[54] which will improve their conductivity and photocurrent response in PEC applications. The optimum measured photocurrent observed for the 3% Mn-doped photoanodes (Figure 8(b)) lies between

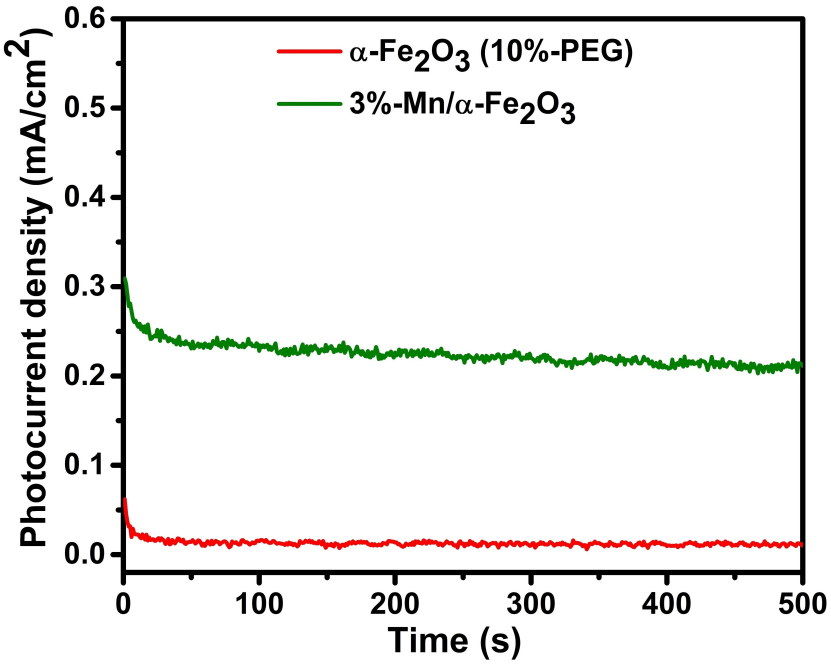

Figure 10. The photostability of (a) undoped α-Fe_2O_3 (10%-PEG) and (b)3%-Mn-doped α-Fe_2O_3 photoanodes.

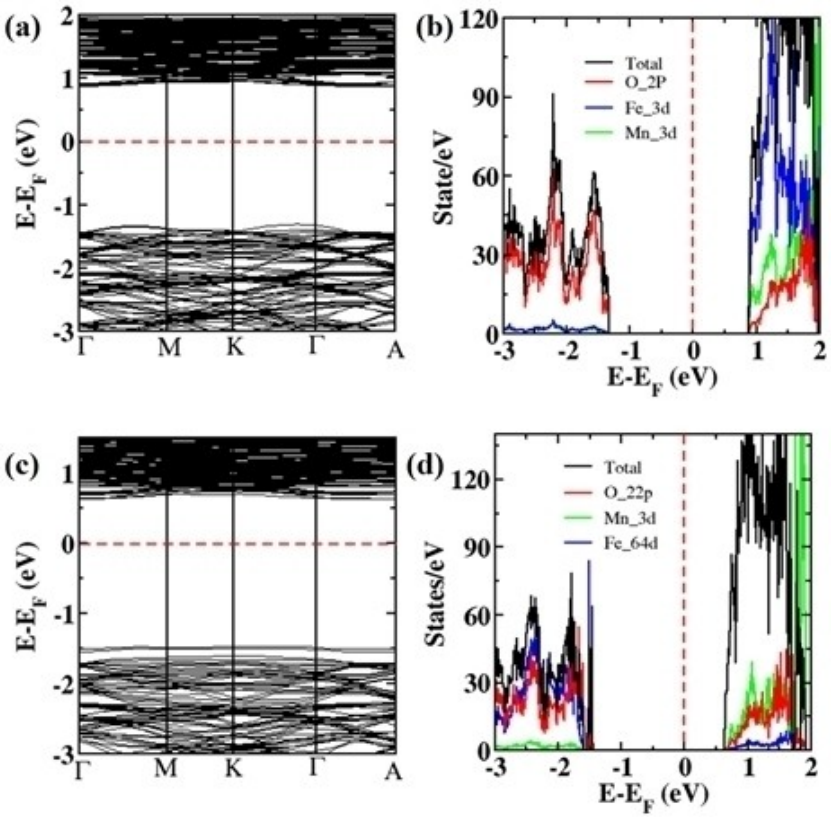

Figure 11. The band structure for (a) 2.1% Mn-doped layer 2 and (c) 4.2% Mn-doped α-Fe_2O_3 systems: (b) and (d) present the PDOS of the systems, respectively. The dashed line denotes the Fermi level of the doped α-Fe_2O_3.

the 2.1 and 4.2% doping levels of the DFT systems and agrees with the band structural analysis results of doped systems. Moreover, no impurity states were observed within the band structure and the PDOS at both doping concentrations of 2.1 and 4.2% at layer 2 of Fe atoms. This is another positive outcome as impurity states in the band structure can act as

locations for recombination of charge carriers during PEC reactions.[49]

A proposed operation mechanism related to charge transport, energy band bending, and PEC reaction occurring on the surface and bulk of Mn-doped α-Fe_2O_3 photoanodes is presented in Figure 12. When the photoanode is dipped into a liquid electrolyte, it eventually attains equilibrium after undergoing some charge transfer processes. The ions in the electrolyte get adsorbed at the photoanode's interface while the electrons around the material's surface are moved toward the solution. This will form a depletion region around the film's surface that is characterized by an electric field.[55] The electric field formed within the depletion region will cause the conduction and valence band (CB and VB) to bend upward. The energy band bending is such that it favors the transfer of holes to the film's surface from the VB and goes against the electrons transport from the CB to the rear FTO contact.[56] Also, a much smaller region of absorbed ions, called the Helmholtz layer, which is adjacent to the surface of the electrode is formed.[55a] During photoelectrocatalysis, the Mn-doped α-Fe_2O_3 photoanodes are illuminated with photons of equal or higher energy than that of the bandgap of the material, which causes the photogeneration of electron-hole pairs. The photogenerated holes are moved from the VB to the surface of the photoanodes, where they oxidize water to produce electrons and release H^+ into the solution. The electrons are transferred from the CB of the photoanodes to the FTO rear contact and moved further to the Pt cathode via the external connection to reduce H^+ to H_2. The inbuilt electric field within the depletion layer accelerates charge carriers' separation, the movement of holes to the photoanode's surface, and the transfer of electrons to the FTO rear contacts. The addition of PEG into the electrolyte enhanced the rate of water oxidation reaction that occurs on the surface of the pristine photoanodes due to the decrease in particle agglomeration, as evident in the improved photocurrent response observed for the 10% PEG samples (Figure 9). The Mn-doping of the pristine films further boosted the water oxidation rate through improved conductivity, charge transport to the surface of the photoanodes, and enhanced charge carriers' separation, leading to the improved photocurrent observed for the films.

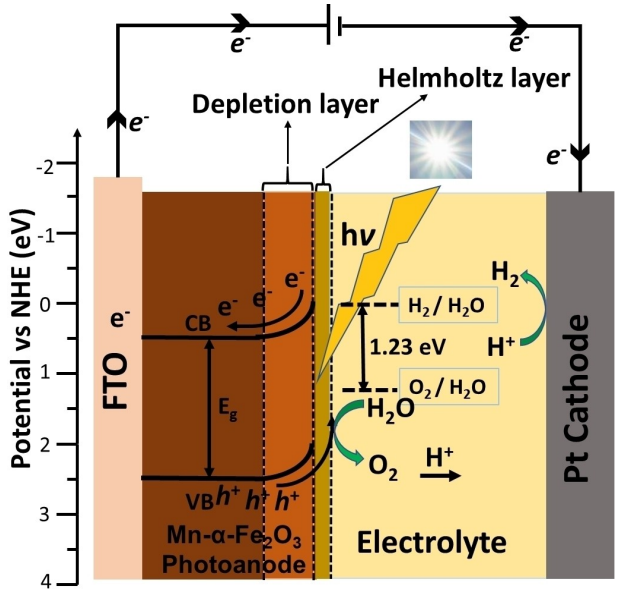

Figure 12. The operation mechanism of Mn-doped α-Fe_2O_3 photoanodes in PEC reactions.

2.4.3. EIS Analysis

EIS studies were conducted on the undoped and doped α-Fe_2O_3 samples to examine the charge transfer dynamics happening in the bulk and at the surface of the films. The results obtained from the EIS studies are given in the Nyquist plots for the undoped and doped samples in Figure 13(a) and (b) respectively. The modeled circuit employed in fitting the EIS data obtained from the measurements is shown in Figure 13(d). Rs, Rbk, and Rct represent the series resistance, the resistance of the trap states in the bulk of the photoanodes, and the resistance to the transfer of charge carriers at the film's surface, respectively. The capacitance in the space charge region of the films is denoted by the constant phase element, CPE1, while CPE2 stands for the surface states capacitance of the photoanodes. The CPE components are made of the pseudo capacitance represented by CPE–T, generally known as the *Q*-value, and a second element, given as CPE–P, with values that can only be between 0 and 1.[57] The CPE components characterize the non-ideal capacitive behavior of the photocathodes and their real capacitance (*C*) values were extracted using Equation 2:[58]

$$C = Q^{1/s} \times R^{(1-s)/s} \quad (2)$$

where *R*, stands for the resistance connected in parallel to the respective CPE elements and *s* is the corresponding CPE–P value. The symbols Cb and Cs denote the actual capacitance values estimated for the CPE1 and CPE2 components, respectively. The estimations made for the various circuit elements of the modeled circuit and the evaluated Cb and Cs values are given in Table 2.

The series resistance, Rs, observed for all the prepared samples produces similar values ranging from 10.45 to 14.33 Ω. This was not expected to differ significantly for the samples as it represents the summation of the ionic resistance in the solution, the resistance in the external wires and the one at the FTO contact,[59] which are uniform for all the samples. The resistance experienced by the trap states within the bulk of the undoped α-Fe_2O_3 films, Rbk, drops with increasing concentration of PEG content in the precursor used for sample preparation, from 70.8 kΩ observed for 0%-PEG samples to 3.3 kΩ for the 10%-PEG films. Meanwhile, the capacitance of the space charge region, Cb, remained relatively constant for the undoped films. At the film's surfaces, the surface states capacitance, Cs, recorded similar values for the undoped samples. However, the resistance to charge transfer, Rct, was observed to reduce with increasing PEG concentration in the

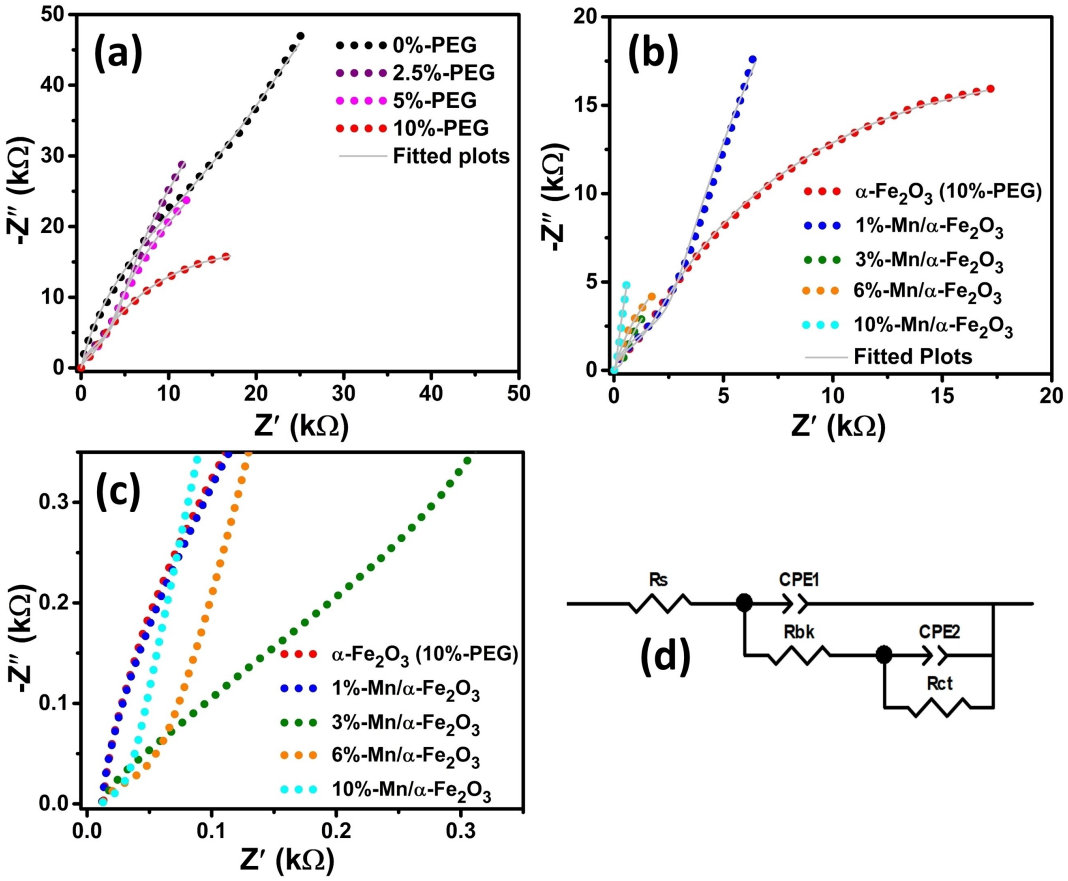

Figure 13. EIS Nyquist plots for (a) undoped and (b) doped α-Fe_2O_3 photoanodes: the modeled circuit employed to fit the raw EIS data is given in (c).

Table 2. The approximate values estimated for the elements in the equivalent circuit that was employed to model the raw EIS data obtained for the α-Fe_2O_3 photoanodes.

Sample	Rs (Ω)	CPE1		Cb (mF)	Rbk (kΩ)	CPE2		Cs (mF)	Rct (kΩ)
		T (mF)	P			T (mF	P		
0%-PEG	10.70	0.019	0.89	0.02	77.82	0.02	0.98	0.02	239.37
2.5%-PEG	10.45	0.020	0.91	0.02	10.10	0.03	0.96	0.03	153.00
5.0%-PEG	10.99	0.022	0.91	0.02	7.00	0.04	0.94	0.04	87.40
10%-PEG	11.88	0.017	0.90	0.01	3.30	0.03	0.86	0.04	37.70
1%-Mn-doped	11.57	0.029	0.90	0.02	5.50	0.06	0.92	0.07	175.00
3%-Mn-doped	13.94	0.168	0.81	0.10	0.64	0.31	0.94	0.34	18.70
6%-Mn-doped	14.33	0.051	0.95	0.04	0.05	0.29	0.88	0.37	22.28
10%-Mn-doped	14.08	0.066	0.97	0.06	0.08	0.25	0.94	0.33	199.44

precursor solution. This was due to the decreasing particle agglomeration observed on the film's surface with increasing PEG content in the solution. Particle aggregates on the film's surface result in a reduced surface-to-volume ratio for the samples, favoring the surface recombination of charge carriers.[37] The improved PEC response observed for the 10%-PEG samples is largely associated with the increased Cs and reduced Rct observed for the films.

For the doped samples, the Rbk and Cb values were not significantly altered by the 1% Mn doping of the films. However, further doping of the films with 3% Mn and above produced a notable decrease in the Rbk value by at least 80.6%, while Cb slightly improved for 6 and 10% Mn-doped films. This means that the trap states for the samples containing 3% Mn doping and above are more probable to get to the surface of the photoanodes during photoelectrocatalysis. The Cs values notably improved for the doped samples with the best values recorded for 3 and 6% Mn-doped samples. The higher Cs value observed for the films indicates a better capacity to accumulate charge carriers at their surfaces during

PEC reactions.[60] In addition, lower Rct values were also observed for the same films, with the least value of 18.7 kΩ estimated for the 3% Mn-doped samples, representing a 50.4% decrease relative to that of the pristine 10%-PEG films. This is more evident in the expanded view of the Nyquist plots for Mn-doped samples shown in Figure 13(c). The reduced Rct and enhanced Cs values observed for the samples are due to the improved conductivity of the films resulting from the doping effect and enhanced charge separation efficiency.[61] This boosted charge separation at the film's surface further accounts for the high photocurrent response observed for the 3% Mn-doped samples. Further doping of the pristine films with 10% Mn led to a sharp increase in the charge transfer resistance by over 5-fold. This is due to the excessive O_2 vacancies created due to the high doping level, which acted as recombination sites for photoexcited charge carriers on the film's surface.[62]

2.5. Formation Energy of α-Fe_2O_3 Systems Doped with Mn

DFT calculations for the formation energies of the doped systems were done to determine their relative thermodynamic stability. The formation energy (E_{form}) calculations were done using Equation 3 in line with the supercell method, following a similar approach from our previous work and other reports.[40a,48,63]

$$E_{form} = E(Mn\ doped) - E(pure) - n\mu_{Mn} + n\mu_{Fe} \quad (3)$$

Where *E(Mn doped)* and *E(pure)* are the total energies of Mn-doped and pristine bulk α-Fe_2O_3 respectively, *n* is the number of Mn atoms in substitution of Fe atoms, and μ_{Mn} and μ_{Fe} are chemical potentials of Mn and Fe in their stable bulk structures respectively. The results of the formation energy evaluated for the Mn-doped α-Fe_2O_3 samples are presented in Table 3. A negative formation energy was obtained for the doped α-Fe_2O_3 in the Fe-rich and O-rich systems. This indicates that the Mn atoms got incorporated into the α-Fe_2O_3 lattice with relative ease and the doped materials are thermodynamically stable:[64] a desired property for PEC applications.

3. Conclusions

In this project, α-Fe_2O_3 photoanodes were electrodeposited on FTO substrates using a modified electrolyte solution that contained 0, 2.5, 5.0, and 10% of PEG 400. In addition, the electrolyte containing 10% PEG was further used to prepare Mn-doped α-Fe_2O_3 films via the addition of 1, 3, 6, and 10% of $MnCl_2.4H_2O$ with respect to the molarity of Fe^{3+} ion source. XRD, Raman, and EDS studies affirm the successful doping of the pristine α-Fe_2O_3 films with Mn. The addition of 10% PEG to the electrolyte notably reduced the agglomeration of α-Fe_2O_3 nanoparticles and produced the best PEC response among the pristine films. The optimum photocurrent density was attained by the photoanodes doped with 3% of the Mn ion source. The films achieved 2.2 and 6.1 times more photocurrent response than the values recorded for the 10%-PEG pristine α-Fe_2O_3 films, at 1.23 and 1.5 V vs RHE respectively. The enhanced PEC response obtained for the doped α-Fe_2O_3 films is associated with increased donor density, reduced flat band potential, and improved charge separation at the solid/liquid junction exhibited by the films. DFT band structure calculations also suggest that the optimal doping level lies in the region of 2.1 and 4.2% of Mn doping, further affirming the measured PEC results. A negative formation energy was obtained for both the undoped and doped α-Fe_2O_3 systems, which indicates that the materials are thermodynamically stable after doping. This research reveals a new pathway for the electrodeposition of doped α-Fe_2O_3 films and emphasizes the roles of Mn-doping in enhancing their PEC response. This research also opens the room for exploring capping agents in the electrodeposition of nanostructured films to limit particle agglomeration.

Table 3. DFT calculated formation energies for the doped α-Fe_2O_3 systems.

Doped α-Fe_2O_3 layer (L)	Formation energy (eV)	
	Fe-rich	O-rich
2.1% Mn-doped L2	−0.89	−3.74
2.1% Mn-doped L3	−0.99	−3.83
4.2% Mn-doped L2	−1.96	−7.65
4.2% Mn-doped L2_3	−2.56	−8.26

Experimental

Electrodeposition of Pristine α-Fe_2O_3 Films

The pristine α-Fe_2O_3 photoanodes were prepared on cleaned FTO substrates using the electrodeposition technique. A method already explained in a previous work was used to clean the FTO substrates.[65] The electrodeposition of the pristine α-Fe_2O_3 films was done using VersaStat 3F potentiostat and an electrochemical cell that uses three electrodes. The FTO/α-Fe_2O_3 acted as the active (working) electrode, while a 2×2 cm platinum mesh and Ag/AgCl immersed in 3 M KCl were engaged as the cathode and reference electrodes respectively. The solution that served as the initial electrolyte was a mixture of 5 mM of $FeCl_3$, 5 mM of KF, 0.1 M of KCl, and 1 M of H_2O_2, dissolved in deionized (DI) water. The electrodeposition was done using the cyclic voltammetry technique, within a potential window of −0.5 and 0.5 V vs. Ag/Cl, at a scan rate of 0.1 V/s, for 65 cycles. This resulted in the deposition of FeOOH films on FTO substrates, which were thoroughly rinsed with DI water and allowed to dry in air. The electrodeposited samples were then calcined in air, at 550°C, for 2 hours to obtain α-Fe_2O_3 films. The sample was labeled 0%-PEG since the electrolyte did not contain PEG 400. More samples were prepared using the same procedure used to prepare the 0%-PEG samples, except that the electrolytes used were made to have 2.5, 5.0, and 10% of PEG 400 relative to the volume of DI water used in the previous electrolyte. The additional samples were denoted as 2.5%-PEG, 5.0%-PEG, and 10%-PEG for the α-Fe_2O_3 films prepared using the electrolytes that contained 2.5, 5.0, and 10% PEG 400 respectively. Further increase of the percentage of PEG 400 in the electrolyte to 20% did not result in the deposition of any significant films. This could be due

to the drop in the conductivity of the electrolyte because of the increase in the PEG 400 (an organic polymer) in the solution.

Electrodeposition of α-Fe_2O_3 Films Doped with Mn

$MnCl_2.4H_2O$ salt was used as the Mn ion source in the electrolyte for the electrodeposition of the Mn-doped α-Fe_2O_3 photoelectrodes. 1, 3, 6, and 10% of $MnCl_2.4H_2O$, calculated by percentage molarity of $FeCl_3$, was added to the solution that contains 10% PEG described in section 4.1 and used as the electrolytes in the electrodeposition of α-Fe_2O_3 electrodes doped with Mn. The same electrodeposition and annealing procedure used for the preparation of the pristine α-Fe_2O_3 films was also engaged in the fabrication of the Mn-doped samples. The films were also annealed at 550 °C to avoid the unintentional thermal diffusion of Sn from the FTO substrates into the Mn-α-Fe_2O_3 films to enable a more precise study of the impact of Mn-doping on the characteristics and PEC response of the photoanodes. The Mn-doped samples prepared using the electrolyte which contained 1, 3, 6, and 10% of $MnCl_2.4H_2O$ were denoted as 1%-Mn-, 3%-Mn-, 6%-Mn-, and 10%-Mn- α-Fe_2O_3 respectively.

Characterization

The phase compositions and other structural properties of the pristine and Mn-doped α-Fe_2O_3 films were investigated using the X-ray diffraction technique, via the engagement of the Bruker D2 PHRASER diffractometer with CuKα radiation of 0.15418 nm wavelength. A WiTec alpha 300 RAS + confocal Raman apparatus set at 5 mW, with an excitation laser of 532 nm, was engaged in conducting Raman spectroscopy measurements on the samples to obtain their vibrational phonon modes. The morphology of the pristine and doped Mn-films and their cross-sectional views were studied using the field emission gun scanning electron microscopy (FEG-SEM) microscopy technique. The Zeiss Ultrafast 540 apparatus was used for these studies and the images obtained were further evaluated by employing the ImageJ tool to extract the grain size and thickness of the films. An Energy Dispersive X-ray Spectroscopy (EDS) facility which was integrated to the SEM apparatus was employed to research the elements present in the pristine and doped α-Fe_2O_3 films. The optical characteristics of the samples were examined using the Ultraviolet–Visible (UV–Vis) spectroscopy technique via the Agilent CARY 60 UV–Vis instrument.

PEC Investigations

A VersaSTAT 3F potentiostat coupled to a three-electrode PEC cell was used to perform electrochemical measurements on the pristine and Mn-doped α-Fe_2O_3 samples. The prepared samples acted as the working photoelectrode in the cell and a 1 M NaOH served as the electrolyte, whereas Ag/AgCl in a 3 M solution of KCl and 4 cm^2 platinum mesh performed the roles of the reference and counter electrodes respectively. The illumination source employed during the PEC data collection was a Newport *Oriel® LCS* – 100™ solar radiation simulator, adjusted to 1 sun with the aid of a standard cell (Newport 91150V). The illumination surface area that the photoanodes were exposed to was 0.49 cm^2. Linear voltammetry measurements were carried out in both dark and light circumstances on the samples, at the rate of 0.05 V/s, to ascertain their photocurrent densities at different potentials. Potentiostatic electrochemical impedance spectroscopy (PEIS) analysis was conducted on the photoelectrodes under illumination at 0.5 V potential against Ag/AgCl, 10000–0.1 Hz, and at an amplitude of 10 mV. ZView software for impedance spectroscopy analysis was used for fitting the PEIS data obtained from the raw analysis to a modeled circuit. A single frequency of 1000 Hz, an AC potential amplitude of 10 mV, and a DC potential interval of −1.1 to 0.6 V vs. Ag/AgCl were used to perform Mott-Schottky investigations on the photoanodes under dark conditions. All illumination was done from the rear sides of the substrates. Equation 4 gives the Nernst relation that was used to transform the potential vs. Ag/AgCl scale to the RHE reference.

$$E_{RHE} = 0.1976V + (0.059 \times pH) + E_{Ag/AgCl} \quad (4)$$

where E_{RHE} denotes the potential vs. RHE scale, 0.1976 V is the estimated value of the potential of Ag/AgCl scale vs. the normal H_2 electrode (NHE) at 25 °C, $E_{Ag/AgCl}$ represents the electrochemical experiments' potential against the Ag/AgCl reference electrode,[26,27] and the pH of the electrolyte used was 13.6.

Computational Methods

DFT method[66] as implemented in quantum-espresso code[67] was engaged to obtain a better understanding of the optical, structural, and electronic properties of the undoped α-Fe_2O_3 and the ones doped with Mn. The valence electrons were described using the Vanderbilt Ultrasoft Pseudopotentials (USPPs),[68] whilst the exchange and correlation energies were handled at the level of the generalized gradient approximation (GGA) of Perdew—Burke–Ernzerhof (PBE).[69] The DFT + U method with the converged U = 5 eV[48] was used to more accurately study the electronic structure of the undoped and Mn-doped systems of α-Fe_2O_3. The expansion of the electronic wave function was done within the plain wave (PW) basis set, using 540 eV as the kinetic energy cut-off. For the force, the threshold for the energy convergence was set to 10^{-5} eV and 10^{-2} eV/Å. The supercell approach was employed to evaluate the effects of Mn-doping on the electronic and stability properties of α-Fe_2O_3. The Monkhorst–Pack (MP) k-point grids[70] of 2×2×1 and 6×6×2 was applied in conducting the Brillouin zone integration for the evaluation of the total energies and the partial density of states (PDOS) respectively, for the supercell of 120 atoms.

Supporting Information

Supporting information is available from the Wiley Online Library or from the author.

Acknowledgements

The authors acknowledge financial support from the University of Pretoria (UP), the externally funded UP postdoctoral fellowship program: grant cost center: A1E689, and the South African Research Chairs Initiative (SARCHI), UID; 115463. The Copperbelt University and the Center for High Performance Computing (CHPC) in Cape Town, South Africa, are also acknowledged for the cluster resources that enabled DFT calculations.

Conflict of Interests

The authors declare no conflict of interest.

Data Availability Statement

The data that support the findings of this study are available from the corresponding author upon reasonable request.

Keywords: Mn-doped α-Fe_2O_3 · electrodeposition · structural properties · PEC response · density functional theory

[1] X. Peng, Q. Jin, *Int. J. Hydrogen Energy* **2022**, *47*, 7569.
[2] Y.-S. Jeong, Y.-K. Choi, B.-S. Kang, J.-H. Ryu, H.-S. Kim, M.-S. Kang, L.-H. Ryu, J.-S. Kim, *Fuel Process. Technol.* **2020**, *198*, 106240.
[3] a) P. I. Kyesmen, N. Nombona, M. Diale, *Adv. Mater. Interfaces* **2023**, *10*, 2300230; b) P. Jubu, F. Yam, P. I. Kyesmen, *Int. J. Hydrogen Energy* **2021**, *46*, 33087.
[4] P. Dias, A. Vilanova, T. Lopes, L. Andrade, A. Mendes, *Nano Energy* **2016**, *23*, 70.
[5] L. Xi, K. M. Lange, *Catalysts* **2018**, *8*, 497.
[6] a) L. Fernandez-Izquierdo, E. L. Spera, B. Durán, R. E. Marotti, E. A. Dalchiele, R. Del Rio, S. A. Hevia, *Molecules* **2023**, *28*, 1954; b) P. I. Kyesmen, N. Nombona, M. Diale, *Mater. Res. Bull.* **2020**, *131*, 110964.
[7] S. Krehula, M. Ristić, M. Reissner, S. Kubuki, S. Musić, *J. Alloys Compd.* **2017**, *695*, 1900.
[8] P. I. Kyesmen, N. Nombona, M. Diale, *J. Alloys Compd.* **2021**, *863*, 158724.
[9] A. G. Hufnagel, H. Hajiyani, S. Zhang, T. Li, O. Kasian, B. Gault, B. Breitbach, T. Bein, D. Fattakhova-Rohlfing, C. Scheu, *Adv. Funct. Mater.* **2018**, *28*, 1804472.
[10] J. S. Nyarige, T. P. Krüger, M. Diale, *Surf. Interfaces* **2020**, *18*, 100394.
[11] T. Fang, L. Li, C. Liu, N. Mitsuzaki, Z. Chen, *J. Photochem. Photobiol. A* **2023**, *434*, 114226.
[12] Z. Landolsi, I. B. Assaker, R. Chtourou, S. Ammar, *J. Mater. Sci. Mater. Electron.* **2018**, *29*, 8176.
[13] a) C. Yilmaz, U. Unal, *RSC Adv.* **2015**, *5*, 16082; b) A. Bak, S. K. Choi, H. Park, *Bull. Korean Chem. Soc.* **2015**, *36*, 1487; c) R. Hessam, P. Najafisayar, *Thin Solid Films* **2019**, *692*, 137633.
[14] P. S. Shinde, G. H. Go, W. J. Lee, *J. Mater. Chem.* **2012**, *22*, 10469.
[15] L. Fu, H. Yu, Y. Li, C. Zhang, X. Wang, Z. Shao, B. Yi, *Phys. Chem. Chem. Phys.* **2014**, *16*, 4284.
[16] M. F. El-Berry, S. A. Sadeek, A. M. Abdalla, M. Y. Nassar, *Inorg. Nano-Met. Chem.* **2020**, *51*, 1418.
[17] K. Kandori, N. Okamoto, T. Ishikawa, *Langmuir* **2002**, *18*, 2895.
[18] a) V. S. Karlashchuk, P. A. Sinitsyn, S. V. Ryazantsev, E. E. Levin, V. A. Nikitina, *J. Electroanal. Chem.* **2024**, *952*, 117957; b) Y. W. Phuan, W.-J. Ong, M. N. Chong, J. D. Ocon, *J. Photochem. Photobiol. C* **2017**, *33*, 54.
[19] L. P. de Souza, R. O. Chaves, A. Malachias, R. Paniago, S. O. Ferreira, A. S. Ferlauto, *J. Appl. Phys.* **2016**, *119*, 245104.
[20] S. Krehula, M. Ristić, Ž. Petrović, L. K. Krehula, I. Mitar, S. Musić, *J. Alloys Compd.* **2019**, *802*, 290.
[21] Gurudayal, S. Y. Chiam, M. H. Kumar, P. S. Bassi, H. L. Seng, J. Barber, L. H. Wong, *ACS Appl. Mater. Interfaces* **2014**, *6*, 5852.
[22] V. Kumar, D. S. Ahlawat, S. A. Islam, A. Singh, *Mater. Sci. Eng. B* **2021**, *272*, 115327.
[23] a) E. L. Tsege, T. S. Atabaev, M. A. Hossain, D. Lee, H.-K. Kim, Y.-H. Hwang, *J. Phys. Chem. Solids* **2016**, *98*, 283; b) E. J. de Melo, J. P. de Mesquita, M. C. Pereira, L. C. Duarte Cavalcante, E. D. Santos Filho, J. Domingos Fabris, J. D. Ardisson, L. C. Alves de Oliveira, *Hyperfine Interact.* **2017**, *238*, 1.
[24] S. S. Ramya, C. Mahadevan, *J. Solid State Chem.* **2014**, *211*, 37.
[25] I. Y. Kaplin, E. S. Lokteva, S. V. Bataeva, K. I. Maslakov, A. V. Fionov, A. V. Shumyantsev, O. Y. Isaikina, A. O. Kamaev, E. V. Golubina, *Pure Appl. Chem.* **2021**, *93*, 447.
[26] R. Nithiyavathi, S. J. Sundaram, G. T. Anand, D. R. Kumar, A. D. Raj, D. A. Al Farraj, R. M. Aljowaie, M. R. Abdel Gawwad, Y. Samson, K. Kaviyarasu, *J. Infect. Public Health* **2021**, *14*, 1893.
[27] M. Hjiri, R. Dhahri, L. El Mir, A. Bonavita, N. Donato, S. Leonardi, G. Neri, *J. Alloys Compd.* **2015**, *634*, 187.
[28] V. Suryawanshi, A. S. Varpe, M. D. Deshpande, *Thin Solid Films* **2018**, *645*, 87.
[29] N. Pattanayak, P. Panda, S. Parida, *Ceram. Int.* **2022**, *48*, 7636.
[30] A. P. Singh, C. Tossi, I. Tittonen, A. Hellman, B. Wickman, *RSC Adv.* **2020**, *10*, 33307.
[31] I. Lorite, J. Romero, J. Fernández, *J. Raman Spectrosc.* **2012**, *43*, 1443.
[32] H. Li, Q. Zhang, C. C. R. Yap, B. K. Tay, T. H. T. Edwin, A. Olivier, D. Baillargeat, *Adv. Funct. Mater.* **2012**, *22*, 1385.
[33] B. Panigrahy, M. Aslam, D. Bahadur, *J. Phys. Chem. C* **2010**, *114*, 11758.
[34] a) S. H. Mir, B. D. Jennings, G. E. Akinoglu, A. Selkirk, R. Gatensby, P. Mokarian-Tabari, *Adv. Opt. Mater.* **2021**, *9*, 2002238; b) D. Ramírez-Ortega, D. Guerrero-Araque, P. Acevedo-Peña, E. Reguera, H. A. Calderon, R. Zanella, *Int. J. Hydrogen Energy* **2021**, *46*, 34333; c) J. Wang, X. Fan, Z. Zhou, K. Tian, *Mater. Sci. Eng. B* **2011**, *176*, 978.
[35] a) C. M. Phan, H. M. Nguyen, *J. Phys. Chem. A* **2017**, *121*, 3213; b) C. V. Restrepo, C. C. Villa, *Environ. Nanotechnol., Monit. Manage.* **2021**, *15*, 100428.
[36] a) K. Asha, V. R. Satsangi, R. Shrivastav, R. Kant, S. Dass, *RSC Adv.* **2020**, *10*, 42256; b) M. Ibadurrohman, K. Hellgardt, *Thin Solid Films* **2020**, *705*, 138009.
[37] F. Pellegrino, L. Pellutiè, F. Sordello, C. Minero, E. Ortel, V.-D. Hodoroaba, V. Maurino, *Appl. Catal. B* **2017**, *216*, 80.
[38] M. Orlandi, A. Mazzi, G. Arban, N. Bazzanella, P. Rudatis, S. Caramori, N. Patel, R. Fernandes, C. A. Bignozzi, A. Miotello, *Electrochim. Acta* **2016**, *214*, 345.
[39] S. Y. Chae, G. Rahman, O.-S. Joo, *Electrochim. Acta* **2019**, *297*, 784.
[40] a) J. Simfukwe, R. E. Mapasha, A. Braun, M. Diale, *MRS Advances* **2018**, *3*, 669; b) H. Pan, X. Meng, G. Qin, *Phys. Chem. Chem. Phys.* **2014**, *16*, 25442.
[41] Y. Liang, C. S. Enache, R. van de Krol, *Int. J. Photoenergy* **2008**, *1*, 739864.
[42] Y. Yang, D. Xu, Q. Wu, P. Diao, *Sci. Rep.* **2016**, *6*, 1.
[43] S. Luo, J. Ke, M. Yuan, Q. Zhang, P. Xie, L. Deng, S. Wang, *Appl. Catal. B* **2018**, *221*, 215.
[44] B. Wickman, A. Bastos Fanta, A. Burrows, A. Hellman, J. B. Wagner, B. landolo, *Sci. Rep.* **2017**, *7*, 40500.
[45] a) K. Sivula, F. Le Formal, M. Grätzel, *ChemSusChem* **2011**, *4*, 432; b) P. I. Kyesmen, N. Nombona, M. Diale, *Front. Energy Res.* **2021**, *9*, 683293.
[46] H.-J. Ahn, M.-J. Kwak, J.-S. Lee, K.-Y. Yoon, J.-H. Jang, *J. Mater. Chem. A* **2014**, *2*, 19999.
[47] a) Y.-H. Chen, K.-J. Tu, *Int. J. Photoenergy* **2012**, *1*, 980595; b) M. Vanags, A. Šutka, J. Kleperis, P. Shipkovs, *Ceram. Int.* **2015**, *41*, 9024.
[48] J. Simfukwe, R. E. Mapasha, A. Braun, M. Diale, *J. Phys. Chem. Solids* **2020**, *136*, 109159.
[49] L. K. Putri, B.-J. Ng, C.-C. Er, W.-J. Ong, W. S. Chang, A. R. Mohamed, S.-P. Chai, *Appl. Surf. Sci.* **2020**, *504*, 144427.
[50] N. M. Ito, W. M. Carvalho, D. N. F. Muche, R. H. R. Castro, G. M. Dalpian, F. L. Souza, *Phys. Chem. Chem. Phys.* **2017**, *19*, 25025.
[51] a) W. Zhang, Y. Zhang, X. Miao, L. Zhao, C. Zhu, *Micromachines* **2024**, *15*, 387; b) S. Kim, M. A. Mahadik, P. Anushkkaran, W.-S. Chae, S. H. Choi, J. S. Jang, *Sustain. Energy Fuels* **2021**, *5*, 3414.
[52] a) F. Feng, C. Li, J. Jian, F. Li, Y. Xu, H. Wang, L. Jia, *J. Power Sources* **2020**, *449*, 227473; b) H. Ma, M. A. Mahadik, J. W. Park, M. Kumar, H. S. Chung, W. S. Chae, G. W. Kong, H. H. Lee, S. H. Choi, J. S. Jang, *Nanoscale* **2018**, *10*, 22560.
[53] a) F. Wu, Y. Chang, W. Zhai, J. Wang, *J. Mater. Sci.* **2022**, *57*, 14936; b) M. Baikov, A. Ponyavina, A. Prishivalko, V. Sviridov, N. Sil'Vanovich, *J. Appl. Spectrosc.* **1996**, *63*, 297.
[54] H. Pan, X. Meng, J. Cai, S. Li, G. Qin, *RSC Adv.* **2015**, *5*, 19353.
[55] a) P. Dias, A. Mendes, *Encyclopedia of Sustainability Science and Technology*, R. A. Meyers, Ed.; Springer Science and Business Media LLC: Berlin/Heidelberg, Germany **2017**, 1; b) C. Jiang, S. J. Moniz, A. Wang, T. Zhang, J. Tang, *Chem. Soc. Rev.* **2017**, *46*, 4645.
[56] E. Kusmierek, *Catalysts* **2020**, *10*, 439.
[57] Y. Gönüllü, K. Kelm, S. Mathur, B. Saruhan, *Chemosensors* **2014**, *2*, 69.
[58] B. Hirschorn, M. E. Orazem, B. Tribollet, V. Vivier, I. Frateur, M. Musiani, *Electrochim. Acta* **2010**, *55*, 6218.
[59] T. Lopes, L. Andrade, F. Le Formal, M. Gratzel, K. Sivula, A. Mendes, *Phys. Chem. Chem. Phys.* **2014**, *16*, 16515.
[60] B. Eftekharinia, A. Moshaii, A. Dabirian, N. S. Vayghan, *J. Mater. Chem. A* **2017**, *5*, 3412.
[61] Y. Phuan, M. Chong, K. Egamparan, B.-K. Lee, T. Zhu, E. Chan, *J. Taiwan Inst. Chem. Eng.* **2016**, *66*, 249.
[62] B. Xin, P. Wang, D. Ding, J. Liu, Z. Ren, H. Fu, *Appl. Surf. Sci.* **2008**, *254*, 2569.
[63] a) Z. Zhou, P. Huo, L. Guo, O. V. Prezhdo, *J. Phys. Chem. C* **2015**, *119*, 26303; b) J. Wang, H. Sun, J. Huang, Q. Li, J. Yang, *J. Phys. Chem. C* **2014**, *118*, 7451.
[64] H. Pan, X. Meng, D. Liu, S. Li, G. Qin, *Phys. Chem. Chem. Phys.* **2015**, *17*, 22179.
[65] P. I. Kyesmen, N. Nombona, M. Diale, *Surf. Interfaces* **2019**, *17*, 100384.

[66] a) P. Hohenberg, W. Kohn, *Phys. Rev.* **1964**, *136*, B864; b) W. Kohn, L. J. Sham, *Phys. Rev.* **1965**, *140*, A1133.
[67] P. Giannozzi, S. Baroni, N. Bonini, M. Calandra, R. Car, C. Cavazzoni, D. Ceresoli, G. L. Chiarotti, M. Cococcioni, I. Dabo, *J. Phys. Condens. Matter* **2009**, *21*, 395502.
[68] D. Vanderbilt, *Phys. Rev. B* **1990**, *41*, 7892.
[69] J. P. Perdew, K. Burke, M. Ernzerhof, *Phys. Rev. Lett.* **1996**, *77*, 3865.
[70] H. J. Monkhorst, J. D. Pack, *Phys. Rev. B* **1976**, *13*, 5188.

Manuscript received: May 2, 2024
Revised manuscript received: June 10, 2024
Version of record online: July 29, 2024